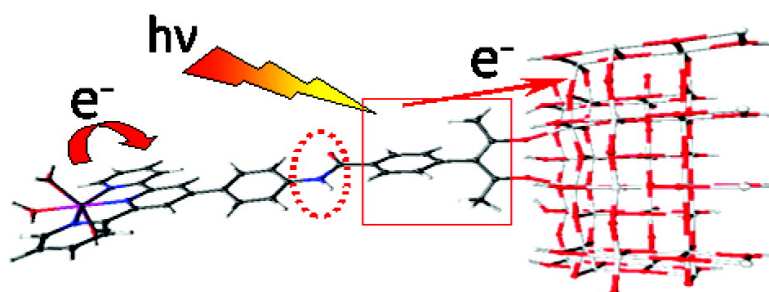**Article**

Acetylacetonate Anchors for Robust Functionalization of TiO Nanoparticles with Mn(II)#Terpyridine Complexes

William R. McNamara, Robert C. Snoeberger III, Gonghu Li, James
M. Schleicher, Clyde W. Cady, Macarena Poyatos, Charles A.
Schmuttenmaer, Robert H. Crabtree, Gary W. Brudvig, and Victor S. Batista

More About This Article

Additional resources and features associated with this article are available within the HTML version:

- Supporting Information
- Access to high resolution figures
- Links to articles and content related to this article
- Copyright permission to reproduce figures and/or text from this article

View the Full Text HTML

Acetylacetonate Anchors for Robust Functionalization of TiO₂ Nanoparticles with Mn(II)−Terpyridine Complexes

William R. McNamara, Robert C. Snoeberger III, Gonghu Li, James M. Schleicher,
Clyde W. Cady, Macarena Poyatos, Charles A. Schmuttenmaer,*
Robert H. Crabtree,* Gary W. Brudvig,* and Victor S. Batista*

Department of Chemistry, Yale University, P.O. Box 208107, New Haven, Connecticut 06520-8107

Received July 15, 2008; E-mail: charles.schmuttenmaer@yale.edu; robert.crabtree@yale.edu; gary.brudvig@yale.edu; victor.batista@yale.edu

Abstract: A novel class of derivatized acetylacetonate (acac) linkers for robust functionalization of TiO₂ nanoparticles (NPs) under aqueous and oxidative conditions is reported. The resulting surface adsorbate anchors are particularly relevant to engineering photocatalytic and photovoltaic devices since they can be applied to attach a broad range of photosensitizers and photocatalytic complexes and are not affected by humidity. Acac is easily modified by CuI-mediated coupling reactions to provide a variety of scaffolds, including substituted terpy complexes (terpy = 2,2′:6,2″-terpyridine), assembled with ligands coordinated to transition-metal ions. Since Mn−terpy complexes are known to be effective catalysts for oxidation chemistry, functionalization with Mn(II) is examined. This permits visible-light sensitization of TiO₂ nanoparticles due to interfacial electron transfer, as evidenced by UV−vis spectroscopy of colloidal thin films and aqueous suspensions. The underlying ultrafast interfacial electron injection is complete on a subpicosecond time scale, as monitored by optical pump-terahertz probe transient measurements and computer simulations. Time-resolved measurements of the Mn(II) EPR signal at 6 K show that interfacial electron injection induces Mn(II) → Mn(III) photooxidation, with a half-time for regeneration of the Mn(II) complex of ca. 23 s.

1. Introduction

Functionalization of metal oxide wide band gap semiconductor surfaces by covalently attaching transition-metal complexes is central in applications to solar energy conversion by dye-sensitized solar cells[1] and photocatalysis.[2,3] Photoinduced interfacial electron transfer (IET) is the fundamental process responsible for advancing the oxidation state of immobilized surface complexes most relevant to these applications. Stabilization of the molecular assembly is achieved by rapid reduction of the photooxidized surface complexes with redox species in solution, preventing recombination by making the back electron transfer several orders of magnitude slower than the forward transfer.[4] In contrast, ensuring robustness and efficient injection under aqueous and oxidative conditions is a more difficult problem that requires design and development of novel linkers and ligands. This article introduces a novel class of derivatized

acetylacetonate (acac) linkers for functionalization of TiO₂ nanoparticles (NPs) and to anchor Mn complexes. It is shown that acac can be synthetically modified, in this case by using CuI coupling reactions, to provide a variety of scaffolds that are robust under aqueous and oxidative conditions and capable of attaching transition-metal catalysts to metal oxide surfaces.

Use of coordination complexes (termed "dyes") that exhibit visible light absorption when attached to metal oxide surfaces has been actively pursued in developing methods of storing solar energy.[5] A variety of anchors for attachment of dyes to metal oxide surfaces have been investigated, including alcohols,[6] diols,[7,8] carboxylic acids,[7,9] silanes,[10] boronic acids,[11] and phosphonates.[12] Currently, the most successful and widely studied dyes are limited to a family of ruthenium bipyridyl complexes that bind to these surfaces through carboxylic acid functional groups such as Ru(dcbpy)₂(NCS)₂, where dcbpy =

(1) (a) O'Regan, B.; Gratzel, M. *Nature* **1991**, *353*, 737–740. (b) Nazeeruddin, M. K.; Kay, A.; Rodicio, I.; Humphrybaker, R.; Muller, E.; Liska, P.; Vlachopoulos, N.; Gratzel, M. *J. Am. Chem. Soc.* **1993**, *115*, 6382–6390.

(2) (a) Serpone, N. *Res. Chem. Intermed.* **1994**, *20*, 953–992. (b) Mills, A.; Leunte, S. *J. Photochem. Photobiol.* **1997**, *108*, 1–35.

(3) Abuabara, S. G.; Cady, C. W.; Baxter, J. B.; Schmuttenmaer, C. A.; Crabtree, R. H.; Brudvig, G. W.; Batista, V. S. *J. Phys. Chem. C* **2007**, *111*, 11982–11990.

(4) (a) Weng, Y. X.; Wang, Y. Q.; Asbury, J. B.; Ghosh, H. N.; Lian, T. Q. *J. Phys. Chem. B* **2000**, *104*, 93–104. (b) Martini, I.; Hodak, J. H.; Hartland, G. V. *J. Phys. Chem. B* **1999**, *103*, 9104–9111. (c) Ghosh, H. N.; Asbury, J. B.; Weng, Y. X.; Lian, T. Q. *J. Phys. Chem. B* **1998**, *102*, 10208–10215. (d) Lu, H.; Prieskorn, J. N.; Hupp, J. T. *J. Am. Chem. Soc.* **1993**, *115*, 4927–4928. (e) Vrachnou, E.; Vlachopoulos, N.; Gratzel, M. *J. Chem. Soc.* **1987**, 868–870.

(5) (a) Connolly, J. S. *Photochemical Conversion and Storage of Solar Energy*; Academic Press: New York, 1981. (b) Gratzel, M. *Energy Resources through Photochemistry and Catalysis*; Academic Press: New York, 1983. (c) Polo, A. S.; Itokazu, M. K.; Iha, N. Y. M. *Coord. Chem. Rev.* **2004**, *248*, 1343–1361.

(6) Zou, C. F.; Wrighton, M. S. *J. Am. Chem. Soc.* **1990**, *112*, 7578–7584.

(7) Notestein, J. M.; Iglesia, E.; Katz, A. *Chem. Mater.* **2007**, *19*, 4998–5005.

(8) Ou, Y.; Lin, J. D.; Zou, H. M.; Liao, D. W. *J. Mol. Catal. A: Chem.* **2005**, *241*, 59–64.

(9) (a) Fujihira, M.; Ohishi, N.; Osa, T. *Nature* **1977**, *268*, 226–228. (b) Nakayama, N.; Hayashi, T. *Colloids Surf., A* **2008**, *317*, 543–550.

(10) Haller, I. *J. Am. Chem. Soc.* **1978**, *100*, 8050–8055.

(11) Altobello, S.; Bignozzi, C. A.; Caramori, S.; Larramona, G.; Quici, S.; Marzanni, G.; Lakhmiri, R. *J. Photochem. Photobiol., A* **2004**, *166*, 91–98.
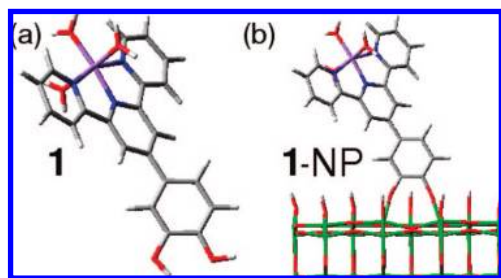
Figure 1. (a) Mn complex **1**: [Mn^{II}(H$_2$O)$_3$(catechol-terpy)]$^{2+}$ (terpy = 2,2′: 6,2″-terpyridine). (b) Surface complex **1**-TiO$_2$-NP. Color scheme: C (gray), H (white), Mn (purple), N (blue), O (red), Ti (green).

Figure 2. (a) Oxidation of catecholate to *o*-quinone. (b) Acetylacetonate scaffold.

(4,4′-dicarboxy-2,2′-bipyridine). This is also known as N719 (also referred to as RuN3 or "red dye") sensitized nanocrystalline TiO$_2$ thin films.[1] The carboxylic acid forms covalent bonds with the TiO$_2$ surface that are stable in anhydrous conditions but undergo hydrolysis in aqueous environments.[14]

In recent work, we demonstrated visible-light sensitization of TiO$_2$ nanoparticles by surface modification with Mn(II)−terpy coordination complexes (Figure 1) using catechol as a linker in aqueous environments.[3] We demonstrated that these Mn complexes can be photooxidized with visible light, using TiO$_2$ nanoparticles as electron acceptors, bypassing the need to consume any sacrificial oxidant. These findings are significant since biomimetic oxomanganese complexes based on terpyridine ligands can be tuned for water splitting,[15] or regio- and stereoselective oxidation of aliphatic CH bonds to form products such as alcohols and epoxides.[13] The demonstration of photooxidation of Mn complexes with visible light, therefore, is essential to bypass the need of primary oxidants and achieve photocatalytic oxidation chemistry based on TiO$_2$ thin films functionalized with Mn catalysts.

Catecholate is a well-established rigid aromatic anchor that stabilizes complex **1** attached to the TiO$_2$ surface, even in aqueous solutions (Figure 1).[3] It facilitates ultrafast electron injection and concomitant Mn(II) → Mn(III) oxidation by linking the Mn complex to the TiO$_2$ NP with favorable electronic couplings and suitable positioning of electronic energy levels.[3] However, the oxidizing power of the resulting Mn(III) complex and the possibility of advancing the oxidation state of the complex to higher valent states are limited by the relatively high electronic states of catechol and the detrimental oxidation pathways, such as formation of *ortho*-quinone, shown in Figure 2a.

In this article, we explore derivatized acac scaffolds, specifically the 2,4-pentanedionate linker substituted at the central carbon as depicted in Figure 2b. A somewhat similar *β*-ketoester anchor was previously reported for a Ru(II) compound (with a 2,2′-bipyridine attached with an *n*-propyl spacer; Figure S3 in the Supporting Information) but provided a less stable linkage than typical carboxylic acids, probably due to unfavorable
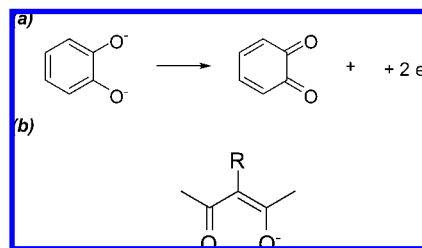
interactions between the surface and 2,2′-bipyridine when attached to the *β*-ketoester via an *n*-propyl that is not derivatizing the central carbon.[16] Therefore, it is important to investigate new derivatized acac scaffolds. Acac is particularly attractive for its ability to form stable coordination complexes with titanium and other metal ions.[17] In particular, Ti(IV) coordination compounds have been extensively investigated in the context of precursors for TiO$_2$ synthesis[18] and are normally stable toward hydrolysis over a wide range of pH conditions.[19] Acac also forms stable adducts with Ti(III)[20] and is expected to be particularly robust during IET. In this article, we investigate these electronic and structural properties and provide evidence for the stability of acac-TiO$_2$ linkages in both aqueous conditions and in the presence of a strong oxidant.

We focus on [Mn^{II}(H$_2$O)$_3$(**2**)]$^{2+}$, where **2**, shown in Scheme 1, is a phenylterpyridine ligand attached to 3-phenyl-acac via an amide bond. The aromatic phenyl substituent on the acac anchor is specifically designed to optimize the rates of IET when linking transition-metal complexes to TiO$_2$ surfaces. The resulting stability in aqueous solutions and under oxidative conditions is expected to be particularly suitable for the accumulation of oxidizing equivalents at the Mn center, without degradation through oxidation pathways. We show that photoexcitation of [Mn^{II}(H$_2$O)$_3$(**2**)]$^{2+}$ bound to TiO$_2$ induces Mn(II) → Mn(III) photooxidation, as probed by EPR at 6 K. Similarly, the regeneration of the Mn(II) complex is monitored by time-resolved measurements of the Mn(II) EPR signal upon blocking the illumination. We also analyze the time scale and reaction mechanism for the underlying ultrafast IET as observed by terahertz (THz) spectroscopy and computer simulations of quantum electronic relaxation. Our results show that this derivatized acac anchor can be used effectively for robust functionalization of colloidal TiO$_2$ NPs and for activating a Mn(II) complex via photoexcitation and IET.

2. Experimental and Computational Procedures

Sample preparation and experimental procedures are described below. All reagents not specifically mentioned were purchased from Aldrich and used without further purification. Ligand synthesis was performed using standard Schlenk techniques under N$_2$ atmosphere.

(12) (a) Gallagher, L. A.; Serron, S. A.; Wen, X. G.; Hornstein, B. J.; Dattelbaum, D. M.; Schoonover, J. R.; Meyer, T. J. *Inorg. Chem.* **2005**, *44*, 2089–2097. (b) Gillaizeau-Gauthier, I.; Odobel, F.; Alebbi, M.; Argazzi, R.; Costa, E.; Bignozzi, C. A.; Qu, P.; Meyer, G. J. *Inorg. Chem.* **2001**, *40*, 6073–6079.
(13) Das, S.; Incarvito, C. D.; Crabtree, R. H.; Brudvig, G. W. *Science* **2006**, *312*, 1941–1943.
(14) (a) Weisz, A. D.; Regazzoni, A. E.; Blesa, M. A. *Croat. Chem. Acta* **2007**, *80*, 325–332. (b) Weisz, A. D.; Regazzoni, A. E.; Blesa, M. A. *Solid State Ionics* **2001**, *143*, 125–130.
(15) Chen, H. Y.; Tagore, R.; Das, S.; Incarvito, C.; Faller, J. W.; Crabtree, R. H.; Brudvig, G. W. *Inorg. Chem.* **2005**, *44*, 7661–7670.

(16) Heimer, T. A.; Darcangelis, S. T.; Farzad, F.; Stipkala, J. M.; Meyer, G. J. *Inorg. Chem.* **1996**, *35*, 5319–5324.
(17) (a) Kessler, V. G.; Gohil, S.; Parola, S. *Dalton Trans.* **2003**, 544–550. (b) Fackler, J. P. *Prog. Inorg. Chem.* **1966**, *7*, 361–378.
(18) (a) Hollingsworth, N.; Kanna, M.; Kociok-Kohn, G.; Molloy, K. C.; Wongnawa, S. *Dalton Trans.* **2008**, 631–641. (b) Kim, Y. T.; Park, Y. S.; Myung, H.; Chae, H. K. *Colloids Surf., A* **2008**, *313*, 260–263.
(19) Sanchez, C.; Babonneau, F.; Doeuff, S.; Leaustic, A. *Ultrastructure Processing of Advanced Ceramics*; Wiley: New York, 1988.
(20) (a) Figgs, B. N.; Lewis, J.; Mabbs, F. *J. Chem. Soc.* **1963**, 2473–2476. (b) Cox, M.; Lewis, J.; Nyholm, R. S. *J. Chem. Soc.* **1965**, 2840–2844.

Scheme 1. Synthesis of Compounds **2** and **3**
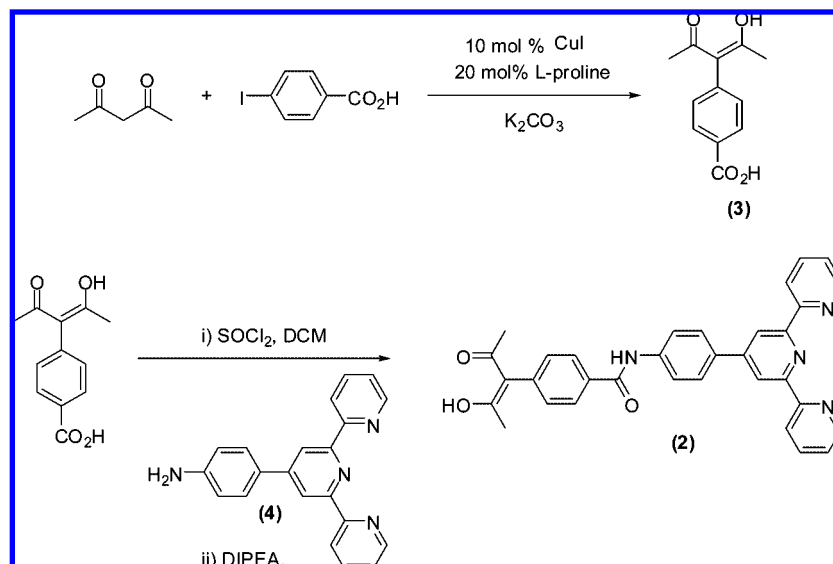
The ^1H and ^{13}C NMR spectra were obtained using Bruker spectrometers operating at 400 and 500 MHz, respectively. Chemical shifts are reported in ppm with the residual solvent as an internal reference. The molecules 3-[4-benzoic acid]pentane-2,4-dione (**3**)[21] and 4′-p-aminophenyl-2,2′:6′,2″-terpyridine (**4**) were synthesized according to literature procedures as shown in Scheme 1.[13] Dichloromethane was dried with a solvent purification system using a 1-m column containing activated alumina. All the other solvents were used as received. The Degussa P25 TiO₂ 25-nm nanoparticles were 70% anatase and 30% rutile.

2.1. Synthesis of 3-[4-Benzoic acid]pentane-2,4-dione (3). Compound **3** was synthesized according to the procedure reported in the literature.[21] A mixture of 4-iodobenzoic acid (1.5 mmol), 2,4-pentanedione (4.5 mmol), K₂CO₃ (7.5 mmol), CuI (0.15 mmol), and L-proline (0.3 mmol) in 15 mL of DMSO was heated at 90 °C under nitrogen atmosphere for 24 h. The cooled solution was poured into 1 M HCl and extracted with ethyl acetate. The organic layer was dried over MgSO₄, and the solvent was removed under vacuum. The crude oil was purified on a silica gel column, using a mixture of hexane/ethyl acetate (1:1) as eluent, to afford 205 mg of **3** (70% yield). ^1H NMR (CDCl₃, 400 MHz): (100% enol form) 16.65 (s, 1H, OH), 8.08 (d, $^3J_{H-H}$ = 8 Hz, 2H, CH$_{Ar}$), 7.25 (d, $^3J_{H-H}$ = 8 Hz, 2H, CH$_{Ar}$), 1.84 (s, 6H, CH₃). ^{13}C NMR (CDCl₃, 75 MHz): 190.7 (C−OH), 171.7 (COOH), 142.8 (C$_{Ar}$), 131.4 (CH$_{Ar}$), 130.8 (CH$_{Ar}$), 128.6 (C$_{Ar}$), 114.5 (C$_{Enol}$), 24.2 (CH₃). MS: ES molecular ion calcd for C₁₂H₁₂O₄H⁺, 221.080835; found, *m/z* = 221.08083.

2.2. Synthesis of 2. Thionyl chloride (0.38 mmol) was added dropwise to a solution of 3-[4-benzoic acid]pentane-2,4-dione (**3**, 0.255 mmol) in dichloromethane (5 mL), and the resulting mixture was refluxed for 3 h. Afterward, the volatiles were removed by bubbling N₂ through the solution. Five milliliters of dry dichloromethane and N,N′-diisopropylethylamine (0.31 mmol) was subsequently added, and the resulting mixture was stirred at room temperature for 10 min. 4′-p-Aminophenyl-2,2′:6′,2″-terpyridine (**4**, 0.255 mmol) was added in 2 mL of dry dichloromethane, and the orange solution was heated for 24 h. The cooled solution was poured into the same amount of water and extracted with ethyl acetate. The organic layer was washed with an aqueous saturated solution of NaHCO₃ and dried over MgSO₄. Upon removal of the volatiles, the oily residue was purified by column chromatography on silica gel. Elution with a 1% MeOH solution in dichloromethane afforded the separation of a colorless band containing compound **2**. Further

elution with a 1% MeOH solution in ethyl acetate afforded the separation of an orange band also containing **2** (60% yield). ^1H NMR (CDCl₃, 400 MHz): % enol (100%) 14.41 (s, 1H, OH), 8.66 (m, 2H, H₅), 8.64 (s, 2H, H₁), 8.58 (d, 2H, $^3J_{H-H}$ = 8 Hz, H₂), 8.19 (br s, 1H, NH), 7.85−7.74 (8H, CH$_{Ar}$ + H₃), 7.27 (qd, 2H, $^3J_{H-H}$ = 7.6 Hz, $^4J_{H-H}$ = 1.2 Hz, H₄), 7.22 (d, $^3J_{H-H}$ = 8.4 Hz, CH$_{Ar}$), 1.81 (s, 6H, CH₃). ^{13}C NMR (CDCl₃, 125 MHz): δ 189.7 (C−OH), 164.3 (CONH), 155.2 (C₁₁), 155.9 (C₁₂), 148.4 (C₉), 148.1 (C₁₆), 139.9 (C₁), 137.8 (C₅), 135.9 (C₁₄), 133.4 (C₈), 133.1 (C₄), 130.6, 127.1, 126.7 (CH$_{Ar}$), 122.8 (C₁₃), 120.4 (C₁₅), 119.4 (C₆), 117.4 (C₁₀), 113.3 (C$_{Enol}$), 13.2 (CH₃). MS: ES molecular ion calcd for C₃₃H₂₆N₄O₃H⁺, 527.207767; found, *m/z* = 527.20636.

2.3. Sensitization of TiO₂ with Complex 2. The samples for time-resolved EPR studies were prepared by stirring 15 mg of Degussa P25 TiO₂ nanoparticles in 2 mL of a 0.9 mM solution of **2** (9.5 mg, 0.018 mmol) in dichloromethane at reflux for 2 h. The resulting suspension was allowed to cool to room temperature and centrifuged to pellet the sensitized nanoparticles. The supernatant was then decanted, and the remaining particles were washed with dichloromethane. The stability of the acac linker was established by exposing the sensitized nanoparticles to an aqueous solution of potassium peroxymonosulfate (oxone). The oxidant did not release the ligand over 5 h.

2.4. Preparation of Mesoporous Thin Films of Sensitized TiO₂. The samples for time-resolved THz and UV−vis spectroscopic measurements consist of thin mesoporous films (∼10-μm thick) of Degussa P25 TiO₂ nanoparticles. The nanoparticles were doctor-bladed from aqueous solution onto a glass coverslip and annealed at 360 °C for 30 min. The resulting slides were sensitized with **2** by refluxing in 60 mL of a 0.03 mM solution (9.5 mg, 0.018 mmol) of **2** in dry dichloromethane for 2 h. The resulting sensitized films were rinsed with dry dichloromethane before analysis. Thin films sensitized with [Mn^{II}(H₂O)₃(**2**)]²⁺ were prepared by rinsing films sensitized with **2** with deionized water and then soaking in a 2 mM aqueous solution of Mn(II) acetate for 12 h.

2.5. UV−vis, FTIR, and Powder X-ray Diffraction Measurements. Films of P25 nanoparticles were highly scattering, and spectra were obtained with a Varian Cary 3 spectrophotometer in diffuse reflectance geometry using an integrating sphere. Nanoparticles prepared by one of the numerous sol-gel methods could provide films of better quality. Reported spectra of nanoparticle films were taken using an NP film on a microscope slide coverslip covered with a drop of pH-neutral deionized water and then with a second coverslip. The baseline spectrum of a coverslip was

(21) Jiang, Y. W.; Wu, N.; Wu, H. H.; He, M. Y. *Synlett* **2005**, *2005*, 2731–2734.

subtracted and only absorbs at wavelengths less than 350 nm. Dry, uncovered samples were also measured and show similar behavior.

Diffuse reflectance infrared Fourier transform spectra were recorded on a Nicolet 6700 infrared spectrophotometer equipped with a DTGS detector and a Nexus Smart Collector. Samples were collected as dry materials and measured in KBr matrix. Typically, 128 scans were performed for each spectrum. The resolution was 2 cm^{-1}. Analogous FTIR methods were previously applied to characterize the binding of carboxylate linkers onto Degussa P25 titania.[22]

The powder X-ray diffraction (XRD) patterns of the samples were recorded on a Bruker-AXS D8 Focus diffractometer ($\lambda =$ 1.5418 Å Cu Kα radiation, step time 1 s) over the range of 20° < 2θ < 60°. The step sizes were 0.05° and 0.02° for P25 and synthesized anatase NPs, respectively.

2.6. Time-Resolved Terahertz Spectroscopy Measurements. An amplified Ti:sapphire laser (Tsunami/Spitfire from Spectra Physics) generated 800 mW of pulsed near-IR light at a 1 kHz repetition rate. The pulse width was ~100 fs, and the center wavelength was 820 nm. Roughly two-thirds of the power was frequency doubled and then filtered to produce 50 mW of 410 nm (3.02 eV) light for the pump beam. The remainder of the near-IR light was used to generate and detect THz radiation using a 4-paraboloid arrangement that focused the THz beam to a spot size of ~3 mm at the sample. Terahertz radiation was generated using optical rectification in a ZnTe(110) crystal and detected using free space electrooptic sampling in a second ZnTe(110) crystal (see Figure S1 in Supporting Information for an experimental diagram). Terahertz data were taken at room temperature with the sample moving to avoid photobleaching. The average of three samples was taken for each data set. Further information on the spectrometer and techniques was reported in the literature.[23,24]

Terahertz radiation was absorbed by mobile electrons in the TiO$_2$ conduction band and was insensitive to electrons within the absorbed sensitizer. A decrease in broadband THz (0.2−2 THz) transmission in photoexcited samples compared to nonphotoexcited samples indicated a higher electron density in the TiO$_2$. Injection time measured by monitoring the change in THz transmission as the delay time between the 410-nm pump and the THz probe was varied.

2.7. EPR Spectroscopy. Perpendicular-mode EPR data were collected on an X-band Bruker Biospin/ELEXSYS E500 spectrometer equipped with an SHQ cavity and an Oxford ESR-900 liquid helium cryostat. All spectra were collected at 6 K on powdered samples sealed in capillary tubes placed in 5-mm o.d. quartz EPR tubes containing 60/40 toluene/acetone which forms a transparent glass for efficient illumination of the sample and allows efficient heat transfer to prevent heating of the sample during illumination (Figure S2 in Supporting Information). All spectra were recorded with the following settings: modulation amplitude = 20 G, modulation frequency = 100 kHz, microwave power = 0.5 mW, and microwave frequency = 9.3863 GHz. Time course measurements follow the signal intensity at 3106 G. All illuminations were carried out in the cryostat with white light passed through 420-nm long-pass and water filters. Relative Mn(II) concentrations are based on comparison of peak-to-peak amplitudes of both initial and illuminated signals at 3147 and 3674 G.

2.8. Water Stability Studies by UV−Vis. Samples of **2**-TiO$_2$ and N719-TiO$_2$ were prepared by stirring mesoporous thin films of Degussa P25 TiO$_2$ nanoparticles in 60 mL of 2 mM solutions of **2** and N719, for 2 h at reflux in dichloromethane and ethanol, respectively. The resulting sensitized TiO$_2$ slides were stirred in deionized neutral pH water for varying lengths of time and measured

using a Varian Cary 3 UV−vis spectrophotometer. Films of P25 TiO$_2$ nanoparticles were highly scattering, and spectra were obtained using an integrating sphere.

2.9. Oxidative Stability Studies by UV−Vis. Samples of **2**-TiO$_2$, N719-TiO$_2$, and catechol-terpy/TiO$_2$ were prepared by stirring mesoporous thin films of Degussa P25 TiO$_2$ nanoparticles in 60 mL of 2 mM solutions of **2**, N719, and catechol-terpy. The resulting slides were then stirred in 2 mM solutions of the primary oxidant oxone for varying lengths of time and measured using a Varian Cary 3 UV−vis spectrophotometer with an integrating sphere.

2.10. Computational Analysis. The description of electron injection involves mixed quantum-classical dynamics simulations of IET in functionalized TiO$_2$ NPs. Simulations of UV−visible photoabsorption spectra are based on TD-DFT electronic structure calculations of model complexes that mimic the attachment of acac adsorbates to TiO$_2$-anatase NPs.

2.10.1. Linker-Anatase Structure. The DFT geometry relaxation of linker-anatase structures was performed by using the Vienna ab Initio Simulation Package (VASP/VAMP)[25] implementing the PW91/GGA[26] approximation in a plane-wave basis and using ultrasoft Vanderbilt pseudopotentials[27] to describe ionic interactions. A wave function cutoff of 400 eV was used in all calculations as well as a single γ point k-point sampling because of the large size of the supercell. The Kohn−Sham (KS) Hamiltonian was projected onto a plane-wave basis set, and high-efficiency iterative methods were implemented to obtain the KS eigenstates and eigenvalues.

Surface reconstruction of the anatase nanostructure induced by functionalization with derivatized acac linkers is described by geometry relaxation of model supercells under vacuum conditions. Supercells were composed of derivatized acac molecules adsorbed on the (101) surface of a TiO$_2$-anatase nanostructure, as depicted in Figure 3. The dimensions of the nanoparticle were 1.0 × 1.5 × 3.1 nm^3 along the [−101], [010], and [101] directions, respectively. Three-dimensional periodic boundary conditions were imposed with a vacuum spacer between slabs, making negligible the interaction between distinct surfaces in the infinitely periodic model system. The surface dangling bonds were saturated with capping hydrogen atoms to quench the formation of surface states[28] and avoid unphysically low coordination numbers. The resulting structural relaxation next to the adsorbate describes the underlying surface reconstruction,[29] a process that partially quenches the formation of surface states deep within the semiconductor band gap.[28]

2.10.2. Surface Complex: Structure. The relaxed structure of [Mn^{II}(H$_2$O)$_3$(**2**)]$^{2+}$ was obtained through DFT minimum-energy geometry optimizations at the B3LYP/(LACVP, 6-31G) level. Structures, including coordination of the acetylacetonate group to a hydrated Ti^{4+} ion, were also obtained in analogy with previously published procedures.[30] All ab initio computations were performed using the programs Jaguar 5.5[31] and Gaussian 03.[32] The full surface complex structure, [Mn^{II}(H$_2$O)$_3$(**2**)]$^{2+}$-NP, was determined by combining the relaxed structure of [Mn^{II}(H$_2$O)$_3$(**2**)]$^{2+}$ with the relaxed supercell of acac adsorbed on anatase.

(22) Mendive, C. B.; Bahnemann, D. W.; Blesa, M. A. *Catal. Today* **2005**, *101*, 237−244.

(23) Baxter, J. B.; Schmuttenmaer, C. A. *J. Phys. Chem. B* **2006**, *110*, 25229−25239.

(24) Beard, M. C.; Turner, G. M.; Schmuttenmaer, C. A. *Phys. Rev. B* **2000**, *62*, 15764−15777.

(25) (a) Kresse, G.; Furthmuller, J. Vienna ab Initio Simulation Package; University of Vienna: Vienna, Austria, 2001. (b) Kresse, G.; Furthmuller, J. *Phys. Rev. B* **1996**, *54*, 11169−11186. (c) Kresse, G.; Furthmuller, J. *Comput. Mater. Sci.* **1996**, *6*, 15−50.

(26) Perdew, J. P. In *Electronic Structure of Solids '91*; Ziesche, P., Eschrig H., Eds.; Akademie Verlag: Berlin, 1991.

(27) Vanderbilt, D. *Phys. Rev. B* **1990**, *41*, 7892−7895.

(28) *Semiconductor Surfaces and Interfaces*; Mönch, W., Ed.; Springer: Berlin, 1993; Vol. 26.

(29) Dieblod, U. *Surf. Sci. Rep.* **2003**, *48*, 53−229.

(30) Duncan, W. R.; Prezhdo, O. V. *J. Phys. Chem. B* **2005**, *109*, 365−373.

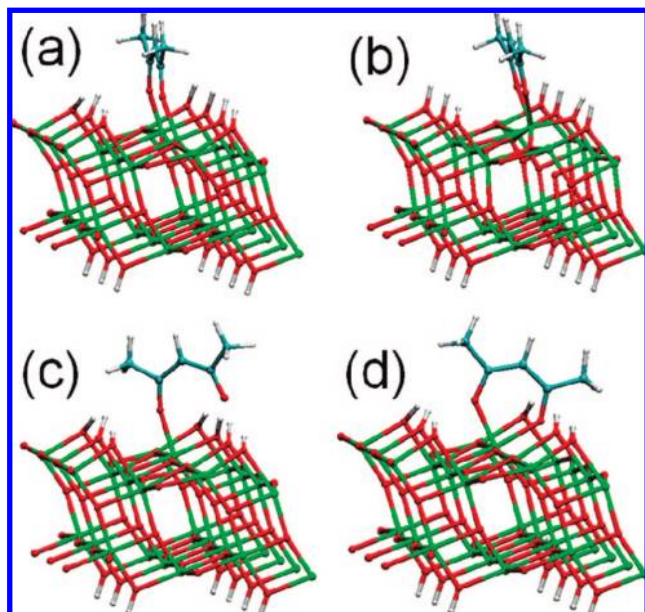(31) Jaguar 5.5; Schrodinger: Portland, OR, 2002.

Figure 3. Comparison of relaxed configurations of model nanostructures of TiO₂-anatase sensitized with: (a) acac anchored to the (101) surface by bridging two Ti⁴⁺ ions, (b) bidentate chelating a single Ti⁴⁺, (c) monodentate binding to a Ti⁴⁺ center, and (d) bidentate chelating a single Ti⁴⁺ at an oxygen vacancy. The binding energies for (a–d) are 42, 12, 47, and 68 kcal/mol, respectively. Green represents Ti⁴⁺ ions, red represents O²⁻ ions, light blue represents C atoms, and small gray spheres represent H atoms.

2.10.3. Functionalized Anatase: Electronic Structure Calculations. The description of the electronic structure of $[Mn^{II}(H_2O)_3(\mathbf{2})]^{2+}$−NP is based on tight-binding model Hamiltonians using the semiempirical extended Hückel (EH) approach, with periodic boundary conditions as implemented in previous work.[3,33−36] It was shown that the method requires a relatively small number of transferable parameters and is capable of providing accurate results for the energy bands of elemental materials (including transition metals) as well as compound bulk materials in various phases.[37] The EH method is applicable to large extended systems and, contrary to plane-wave basis set approaches, provides valuable insight on the role of chemical bonding.[36] The method is, therefore, most suitable to develop a clear chemical picture of the relative positioning of electronic energy levels, at the semiquantitative level, and the electronic couplings responsible for the IET mechanism.[3,33−35]

2.10.4. Simulations of IET. We computed the survival probability, $P(t)$, defined as the probability that the photoexcited electron remains in the adsorbate molecule at time t after excitation of the system.[33] $P(t)$ characterizes the IET time scales and was obtained as the projection of the time-evolved electronic wave function onto the atomic orbitals (AOs) of the molecular adsorbate. Computing the time-dependent wave function $|\Psi(t)\rangle = \sum_i B_i(t)|\chi_i\rangle$, expanded in the basis set of AOs $|\chi_i\rangle$, required the propagation of the expansion coefficients $B_i(t) = \sum_q Q_i^q C_q \exp[-(i/\hbar)E_q t]$, where C_q is the expansion coefficient of the initial state $|\Psi(0)\rangle = \sum_q C_q|q\rangle$. The eigenvectors and eigenvalues Q^q and E_q were obtained by solving the generalized EH eigenvalue problem, $HQ^q = E_q SQ^q$, with H the EH Hamiltonian matrix. Here, S is the atomic orbital overlap matrix. Once the time-dependent wave function was obtained, the survival probability was computed as follows: $P(t) = |\sum_i^{MOL} \sum_j B_i^*(t)B_j(t)S^{ij}|$. To avoid artificial recurrences in electron-transient populations, the calculations of charge injection were conducted in models consisting of a 3×3 adsorbate-anatase supercell array. Initial states are defined in terms of the excited electronic states of the adsorbate with significant electronic couplings with the semiconductor conduction band.

2.10.5. Simulations of UV−Vis Spectra. Figure 6 shows the UV−vis spectrum of the complex $[Ti(phenyl-acac)(H_2O)_4]^{3+}$, as obtained at the TD-DFT/(LACVP, 6-31G) level of theory. The infinite resolution spectrum described by the oscillator strengths of vertical transitions, associated with the complex in the ground-state minimum energy configuration, is compared to the spectrum convoluted with a Gaussian function (fwhm = 60 nm) to mimic inhomogeneous broadening induced by thermal nuclear fluctuations. Note that the phenyl-acac in such a model complex is acting as a bidentate ligand, modeling adsorption at an oxygen vacancy (Figure 3d). These calculations suggest that functionalization of TiO₂ surfaces with phenyl-acac should lead to visible-light sensitization due to ligand-to-metal and intraligand transitions at $\lambda < 550$ nm. These electronic transitions are common to other Lewis base anchors attached to TiO₂ (e.g., catechol[3]) and can be exploited for absorption of visible light even when the anchor/linker and the TiO₂ surface absorb only in the UV region of the spectrum.

3. Results

The results are presented in six subsections. First, we analyze the acac-TiO₂ binding energy and configuration. Second, we characterize the density of electronic states. Third, we analyze the stability of acac-TiO₂ surface complexes sensitizing TiO₂ NPs in aqueous conditions, in an effort to investigate the stability of derivatized acac linkers in aqueous solutions as compared to carboxylate linkers typically used in dye-sensitized solar cells. Fourth, we analyze the stability of the surface complexes under oxidative conditions. Fifth, we analyze the dynamics of ultrafast IET as characterized by THz spectroscopy and direct comparisons with quantum dynamics simulations. Finally, the sixth section characterizes the dynamics of photooxidation of the Mn center induced by visible light, as probed by time-resolved EPR spectroscopy.

3.1. Acac-Anatase Structure and Binding Energy. Figure 3 shows relaxed configurations of TiO₂-anatase nanostructures, functionalized with acac on the (101) surface, after fully optimizing the energy of the system with respect to the geometry of the anchored molecule and the six topmost layers of the semiconductor surface. Our computational analysis was focused on the (101) surface of anatase since the XRD analysis indicates that Degussa P25 is 85% anatase, with the large diffraction contribution from the (101) surface. In addition, we also observe

(32) Frisch, M. J.; Trucks, G. W.; Schlegel, H. B.; Scuseria, G. E.; Robb, M. A.; Cheeseman, J. R.; Montgomery, J. A., Jr.; Vreven, T.; Kudin, K. N.; Burant, J. C.; Millam, J. M.; Iyengar, S. S.; Tomasi, J.; Barone, V.; Mennucci, B.; Cossi, M.; Scalmani, G.; Rega, N.; Petersson, G. A.; Nakatsuji, H.; Hada, M.; Ehara, M.; Toyota, K.; Fukuda, R.; Hasegawa, J.; Ishida, M.; Nakajima, T.; Honda, Y.; Kitao, O.; Nakai, H.; Klene, M.; Li, X.; Knox, J. E.; Hratchian, H. P.; Cross, J. B.; Bakken, V.; Adamo, C.; Jaramillo, J.; Gomperts, R.; Stratmann, R. E.; Yazyev, O.; Austin, A. J.; Cammi, R.; Pomelli, C.; Ochterski, J. W.; Ayala, P. Y.; Morokuma, K.; Voth, G. A.; Salvador, P.; Dannenberg, J. J.; Zakrzewski, V. G.; Dapprich, S.; Daniels, A. D.; Strain, M. C.; Farkas, O.; Malick, D. K.; Rabuck, A. D.; Raghavachari, K.; Foresman, J. B.; Ortiz, J. V.; Cui, Q.; Baboul, A. G.; Clifford, S.; Cioslowski, J.; Stefanov, B. B.; Liu, G.; Liashenko, A.; Piskorz, P.; Komaromi, I.; Martin, R. L.; Fox, D. J.; Keith, T.; Al-Laham, M. A.; Peng, C. Y.; Nanayakkara, A.; Challacombe, M.; Gill, P. M. W.; Johnson, B.; Chen, W.; Wong, M. W.; Gonzalez, C.; Pople, J. A. Gaussian 03, revision C.02; Gaussian, Inc.: Wallingford, CT, 2004.
(33) Rego, L. G. C.; Batista, V. S. *J. Am. Chem. Soc.* **2003**, *125*, 7989–7997.
(34) Abuabara, S. G.; Rego, L. G. C.; Batista, V. S. *J. Am. Chem. Soc.* **2005**, *127*, 18234–18242.
(35) (a) Rego, L. G. C.; Abuabara, S. G.; Batista, V. S. *J. Chem. Phys.* **2005**, *122*, 154709. (b) Rego, L. G. C.; Abuabara, S. G.; Batista, V. S. *Quantum Inf. Comput.* **2005**, *5*, 318–334. (c) Rego, L. G. C.; Abuabara, S. G.; Batista, V. S. *J. Mod. Opt.* **2006**, *53*, 2519–2532.
(36) Hoffman, R. *Rev. Mod. Phys.* **1988**, *60*, 601–628.
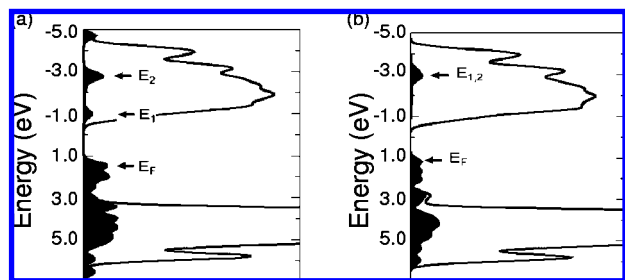(37) Cerda, J.; Soria, F. *Phys. Rev. B* **2000**, *61*, 7965–7971.

Figure 4. The Density of states (DOS) of the TiO₂ anatase nanostructure functionalized with phenyl-acac (a) and catechol (b), bridging between two Ti^{4+} ions on the (101) surface. The filled solid curve represents the DOS projected on the basis functions of the adsorbate. The Fermi energy E_F indicates the HOMO of the system, while states E_1 and E_2 represent the excited electronic states with a predominant contribution of the phenyl-acac-LUMO and phenyl-acac-(LUMO + 1), respectively. The distribution of eigenstates is convoluted with a Gaussian (fwhm = 0.5 eV) to facilitate the visualization of electronic energy bands.

a predominant diffraction contribution from the (101) anatase surface in amorphous and crystalline anatase synthesized by sol−gel methods (our XRD data is provided in the Supporting Information and is consistent with recently reported studies[38]).

Four binding modes are compared, including (a) bridging two different Ti^{4+} ions on the (101) surface, (b) chelating a single Ti^{4+} ion, (c) monodentate coordination to a single Ti^{4+} ion, and (d) chelating a four-coordinate Ti^{4+} ion at an oxygen defect. The binding energies are 42, 12, 47, and 68 kcal/mol, respectively. These calculations indicate that acac attaches strongly to pristine (101) TiO₂ surfaces (i.e., no oxygen vacancy) when anchored via the bridging mode (a) or the monodentate coordination (c). Binding according to the chelating mode (b), however, is 30−35 kcal/mol less stable because of the resulting displacement of the anchoring Ti^{4+} ion away from the (101) surface. However, these calculations find that the most stable attachment corresponds to acac adsorption to surface bridge-bonded oxygen vacancies that are common surface defects in TiO₂.[29,39] Figure 3d shows acac binding to such an oxygen vacancy site, chelating the four-coordinate Ti^{4+} ion. It is shown that the absence of the surface oxygen allows acac to form a robust six-membered ring with the Ti^{4+} ion, without inducing significant structural rearrangements as observed in binding mode (b) (Figure 3b).

The calculated binding energies of acac in the various coordination modes suggest that, under low coverage conditions, acac must block surface oxygen vacancies, as a bidentate ligand to Ti^{4+} ions as depicted in Figure 3d. At higher surface coverages, surface oxygen vacancies will be saturated and acac will bind in modes (a) and (c) as depicted in Figure 3a,c, according to the bridging and monodentate coordination modes. Upon surface reconstruction, however, the coordination of acac is expected to change, stabilizing the formation of surface oxygen vacancies.

3.2. Density of Electronic States. Figure 4 shows the comparison of the DOS of TiO₂ anatase nanostructures functionalized with phenyl-acac and catechol linkers.[40] The filled solid curve in Figure 4 represents the projected density of states on the adsorbate basis functions, showing that strong Lewis bases such as acac and catechol bind to the surface and introduce
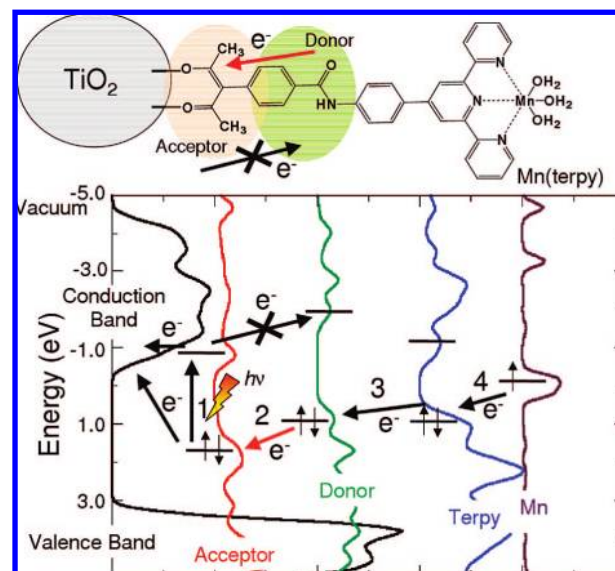

Figure 5. Top: Schematic diagram of a TiO₂ NP functionalized with [Mn^{II}(H₂O)₃(**2**)]$^{2+}$, where the Mn complex is covalently attached to the TiO₂ surface by the phenyl-acac anchor. Bottom: Density of electronic states, convoluted with a Gaussian (fwhm = 0.5 eV) to facilitate the visualization of electronic energy bands. The arrows indicate the electron transfer pathway, induced by photoexcitation and electron injection, leading to Mn oxidation. Favorable directionality of electron transfer is due to the positioning of electronic energy levels in the electron donor and acceptor parts of the ligand-linker chromophore.

electronic states in the semiconductor band gap. The Fermi level of phenyl-acac/TiO₂ structure is lower than the corresponding state in catechol/TiO₂, suggesting that phenyl-acac/TiO₂ should be more robust under oxidative conditions. Furthermore, the lower lying E_1 state in phenyl-acac/TiO₂ relative to that for catechol/TiO₂ should allow for excited-state IET from a wider range of molecular complexes. The additional electronic states in the TiO₂ band gap lead to visible-light sensitization when they are optically coupled to the electronic states at the bottom of the conduction band (e.g., states with predominant contributions from the 3d$_{xz}$, 3d$_{yz}$, and 3d$_{xy}$ orbitals of Ti^{4+} ions directly coordinating the adsorbate molecules). These interfacial electronic state transitions lead to oxidation of the attached molecular complexes, as illustrated in Figure 5.

Figure 5 shows that the excited electronic states of the [Mn^{II}(H₂O)₃(**2**)]$^{2+}$ (e.g., the excited electronic states E_1 and E_2 with predominant contributions of the phenyl-acac-LUMO and phenyl-acac-(LUMO + 1), respectively) overlap with the conduction band. These states can therefore mediate excited-state IET when the anchoring complex is photoexcited. The density of states and the component projections into basis functions of the linkers suggest that the phenyl-acac/TiO₂ surface should be resistant to oxidation because of the low-lying electronic states, should allow for visible light sensitization because of cross electronic transitions to the TiO₂ conduction band, and should lead to photooxidation of the attached molecular complexes because of the favorable relative positioning of the electronic energy levels.

(38) Yeredla, R. R.; Xu, H. *Nanotechnology* **2008**, *19*, 055706.
(39) (a) Kim, Y. K.; Kay, B. D.; White, J. M.; Dohnalek, Z. *Surf. Sci.* **2008**, *602*, 511−516. (b) Kim, Y. K.; Kay, B. D.; White, J. M.; Dohnalek, Z. *Catal. Lett.* **2007**, *119*, 1−4.
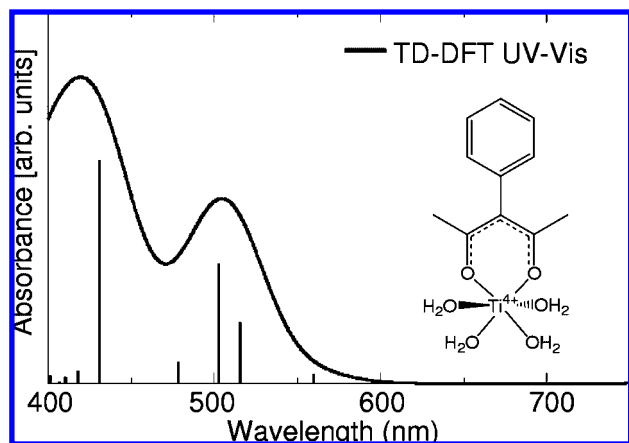
(40) (a) McGlynn, S. P.; Vanquickenborne, L. G.; Kinoshita, M.; Carroll, D. G. *Introduction to Applied Quantum Chemistry*; Holt, Rinehart, and Winston: New York, 1972. (b) Nalewajski, R. F.; Koster, A. M.; Bredow, T.; Jug, K. *J. Mol. Catal.* **1993**, *82*, 407−423. (c) Bredow, T.; Jug, K. *Surf. Sci.* **1995**, *327*, 398−408. (d) Bredow, T.; Jug, K. *J. Phys. Chem.* **1995**, *99*, 285−291. (e) Kormann, C.; Bahnemann, D. W.; Hoffmann, M. R. *J. Phys. Chem.* **1988**, *92*, 5196−5201.

Figure 6. UV−vis spectrum of the complex [Ti(phenyl-acac)(H₂O)₄]³⁺ shown in the inset, obtained at the TD-DFT/(LACVP, 6-31G*) level of theory.
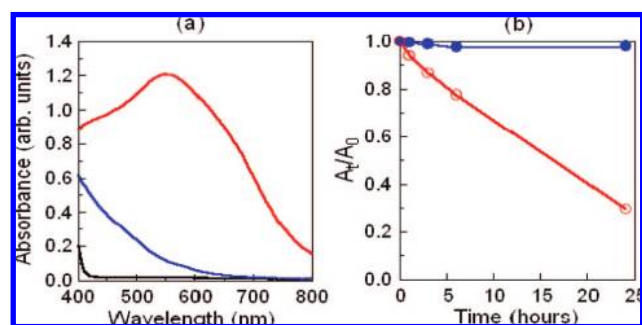

Figure 7. (a) Comparison of the UV−vis spectra of P25 TiO₂ NPs sensitized with **2** (blue), N719 (red), and bare P25 TiO₂ (black). (b) Comparison of the amount of sensitizers that remained attached to TiO₂ as a function of time of incubation in water, based on the absorbance at time *t* relative to the initial absorbance (*t* = 0). 450 and 550 nm were used as the characteristic wavelengths for **2**-TiO₂ (blue) and N719-TiO₂ (red), respectively.

3.3. Water Stability Studies by UV−Vis Spectroscopy.

Figure 7a compares UV−vis spectra of [Mn^{II}(H₂O)₃(**2**)]²⁺ linked to P25 TiO₂ NPs with N719-sensitized TiO₂ NPs as well as bare TiO₂ NPs. Several spectra were collected after immersing the samples in water for 0−24 h, and the absorbance at a specific wavelength for the dye-sensitized samples relative to that before soaking is shown in Figure 7b. Note that the absorbance of [Mn^{II}(H₂O)₃(**2**)]²⁺ linked to P25 TiO₂ NPs remains relatively unchanged, even after being stirred in water for a period of 24 h. On the other hand, Figure 7b shows that the absorbance of the N719-sensitized TiO₂ NPs decreases significantly as a function of time in water, reaching roughly 0.3 after 24 h. These results demonstrate the detachment of carboxylate linkers from the TiO₂ surface in the presence of water and that the acac linkage is highly resistant to detachment under aqueous conditions.

3.4. Stability under Oxidative Conditions.

We compared functionalized TiO₂ thin films before and after treatment with a 2 mM solution of aqueous oxone for 24 h. We found that TiO₂ surfaces functionalized with derivatized acac were relatively unaffected by aqueous oxone, indicating that the acac-TiO₂ linkage is robust under aqueous and oxidative conditions. In contrast, TiO₂ thin films functionalized with terpy-catechol ligands and carboxylate linkers were significantly degraded when exposed to oxone.

Figure 8a,b show UV−vis spectra of **2**- and N719-sensitized TiO₂ thin films, respectively, after exposure to 2 mM oxone
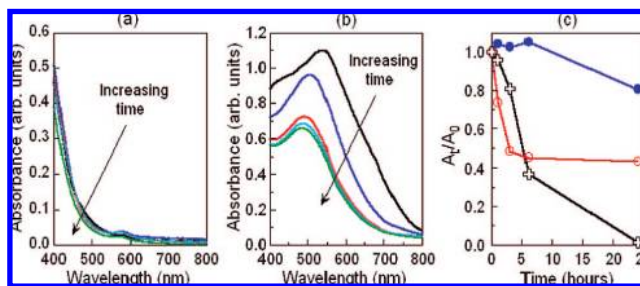

Figure 8. (a, b) UV−vis spectra of **2**-TiO₂ and N719-TiO₂, respectively, after exposure to 2 mM oxone for 0 (black), 1 (blue), 3 (red), 6 (light green), and 24 (green) hours. Analogous spectra for terpy-catechol/TiO₂ are provided in the Supporting Information. (c) Decrease in absorbance as a function of time of TiO₂ thin films functionalized with N719 (red, measured at 550 nm), catechol-terpy (black, measured at 450 nm), and **2** (blue, measured at 450 nm) due to exposure to 2 mM aqueous oxone.
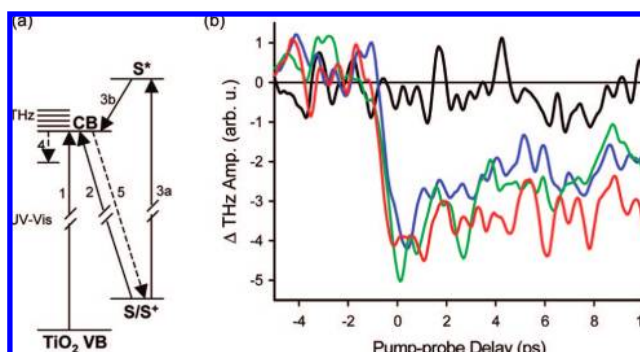

Figure 9. (a) Schematic of possible electron injection pathways into TiO₂ from bulk photoexcitation (1) or from photoexcitation of the sensitizer, S/S* (2 and 3). Electrons can also become trapped in TiO₂ (4) and recombine with the oxidized sensitizer (5). Processes 1−3 decrease THz transmission, whereas 4 and 5 increase it. (b) 410-nm pump/THz probe of electron injection in functionalized TiO₂ NP films of the following: N719 (red), **2** (blue), and [Mn^{II}(H₂O)₃(**2**)]²⁺ (green).

for 0−24 h. A shift in the absorption maximum of the N719-sensitized TiO₂ spectrum after exposure to 2 mM oxone for 1 (blue), 3 (red), 6 (light blue), and 24 (green) hours suggests decomposition of the dye under aqueous oxidative conditions. No such spectral shift in absorbance is observed for **2**-TiO₂, indicating robustness of **2**. In addition, Figure 8c shows the decrease in absorbance for TiO₂ NP thin films functionalized with N719 (red), catechol-terpy (black), and **2** (blue), as a function of time exposure to 2 mM aqueous oxone. It is clear that derivatized acac scaffolds are much more robust than carboxylate and catechol linkers under prolonged exposure to aqueous oxidative conditions.

3.5. Ultrafast Interfacial Electron Transfer.

Since THz radiation is absorbed by free electrons in the TiO₂ conduction band, it is possible to compare the time scale and efficiency of charge injection into bare and functionalized TiO₂ NPs with subpicosecond temporal resolution.[23,41] Photoexcitation and subsequent electron injection causes the free carrier population in the TiO₂ to increase, decreasing the THz transmission amplitude.

Figure 9a shows possible electron injection pathways into TiO₂ from bulk photoexcitation or from photoexcitation of the sensitizer, S/S*. There are three possible pathways for electrons to be injected into the TiO₂ conduction band since the photoexcitation energy of the pump−pulse is near the band edge of the TiO₂. These include (1) direct photoexcitation of bulk

---

(41) Schmuttenmaer, C. A. *Chem. Rev.* **2004**, *104*, 1759–1779.

TiO$_2$, (2) direct transitions from the sensitizer into the TiO$_2$ conduction band, and (3) photoexcitation of the sensitizer, followed by relaxation to the TiO$_2$ conduction band. In cases (2) and (3), the sensitizer could inject from orbitals localized on the phenyl-acac part of the linker or from orbitals localized in the Mn−terpy complex. Each of these pathways lead to the creation of Mn(III), since even injection from the phenyl-acac linker is followed by the subsequent oxidation of Mn(II) and linker reduction by electron transfer as shown in Figure 5.

Figure 9b shows ultrafast interfacial electron injection induced by 410-nm photoexcitation of TiO$_2$ NP colloidal thin films, including bare TiO$_2$, and TiO$_2$ NPs functionalized with $[Mn^{II}(H_2O)_3(\textbf{2})]^{2+}$, **2**, and N719. There is negligible THz absorption from the bare TiO$_2$ sample, which is consistent with its negligible absorption at 410 nm. The magnitudes of the changes in THz transmission through NP films sensitized with each of the three adsorbates are essentially the same, which confirms charge injection from the photoexcited sensitizer via pathways (2) and/or (3). Although the transmission unit in Figure 9b is arbitrary, the same scaling factor is used for all spectra, so amplitude comparisons are meaningful (i.e., no normalization was performed).

The ultrafast spectroscopic data (Figure 9b) indicate that IET from the adsorbate to the NP is completed on a subpicosecond time scale after photoexcitation of the system. The time-resolved THz injection data are well fit using a single exponential with time constant of ∼300 fs convoluted with a Gaussian instrument response function for each of the sensitizers. We note that 300 fs actually represents an upper bound on the injection time scale, since this approaches the limit of the time resolution of ∼500 fs for the spectrometer. Additionally, THz radiation is only sensitive to mobile electrons. If injected electrons are initially bound at surface sites[42] or exhibit low mobility before thermalizing with the TiO$_2$ lattice,[43] they will be invisible or less visible to the THz probe.[24] The 300 fs should then correspond to the time for electrons to become highly mobile, while the time scale for interfacial electron injection is probably much faster. THz measurements taken over hundreds of picoseconds do not show any slower injection components for any of the sensitizers. However, we cannot exclude the possibility that there are multiple time scales for injection from the various pathways mentioned previously, but that all time scales are equal to or faster than our experimental resolution.

Figure 9b also shows that the THz absorbance signal decays exponentially with a half-life of ∼10 ps for each of the three sensitizers and then levels off. This indicates that the injected electrons get trapped at TiO$_2$ defects or surface sites or recombine with oxidized adsorbates. However, the Mn(III) created by photooxidation of $[Mn^{II}(H_2O)_3(\textbf{2})]^{2+}$ could remain stable for much longer since the photogenerated electron and hole are no longer correlated. Previous experiments show recombination in sensitized NP systems to occur on time scales ranging from picoseconds to milliseconds,[44] and the lifetimes of the electron and the Mn(III) are expected to depend strongly on the composition of the solution surrounding the NP film.

Figure 10 (top) shows the time-dependent adsorbate populations obtained by solving the electronic time-dependent Schrödinger equation according to a mixed quantum-classical
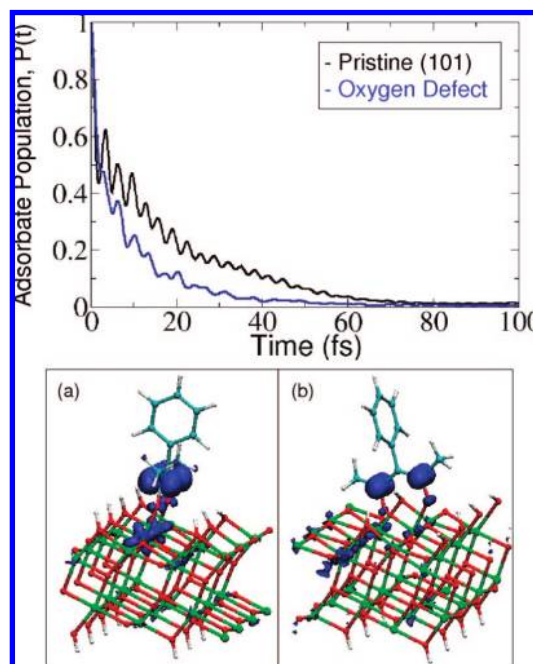
(42) Gundlach, L.; Ernstorfer, R.; Willig, F. *Phys. Rev. B* **2006**, *74*, 035324.
(43) Turner, G. M.; Beard, M. C.; Schmuttenmaer, C. A. *J. Phys. Chem. B* **2002**, *106*, 11716–11719.
(44) Ramakrishna, G.; Ghosh, H. N. *J. Phys. Chem. B* **2001**, *105*, 7000–7008.

Figure 10. Top: Time-dependent adsorbate populations corresponding to photoexcited surface complexes attached to a pristine (101) surface (black) or an oxygen vacancy (blue). Bottom: Snapshots of the electronic charge distribution at 10 fs after initiating the IET from phenyl-acac attached to a pristine (101) surface (a) or attached to an oxygen vacancy defect (b). Only the TiO$_2$ structure next to photoexcited adsorbate is shown for a detailed view of the Ti^{4+} d orbitals localizing the injected charge during the early time IET.

approach.[3,33,34] These transient adsorbate populations are obtained by projecting the time-evolved electronic wave packet onto the atomic orbitals of the molecular adsorbate. These results indicate that typical electron injection events are completed within 50−100 fs for linkers attached to pristine surfaces or oxygen vacancies. These results are consistent with our THz spectroscopic measurements since the predicted time scale for electron injection is shorter than the ∼500 fs instrument response function.

Figure 10 (bottom) shows the distribution of injected charge, at the molecular level, 10 fs after excitation of the $[Mn^{II}(H_2O)_3(\textbf{2})]^{2+}$−NP surface complex to a representative electronic excited state that overlaps with electronic states in the semiconductor conduction band (see state E$_1$ in Figure 4). Several other electronic states also play an important role in the process of electron injection, including states localizing the electronic excitation around the anchoring site, and others localizing the excitation around the phenyl, or terpy, moieties. Most of these photoactive states show similar early time relaxation leading to depletion of electronic density in the linker and electron injection into the d$_{xz}$ orbitals of Ti^{4+} ions next to the surface complex, followed by charge diffusion and surface-charge separation in the conduction band.

The THz measurements, in conjunction with the simulations of IET, show the directional character of IET where injection, rather than intraligand relaxation, is clearly the preferred pathway. Examining the mechanism of IET at this level of detail also supports earlier conclusions about the crucial role of electronic couplings, rather than nuclear reorganization, as the
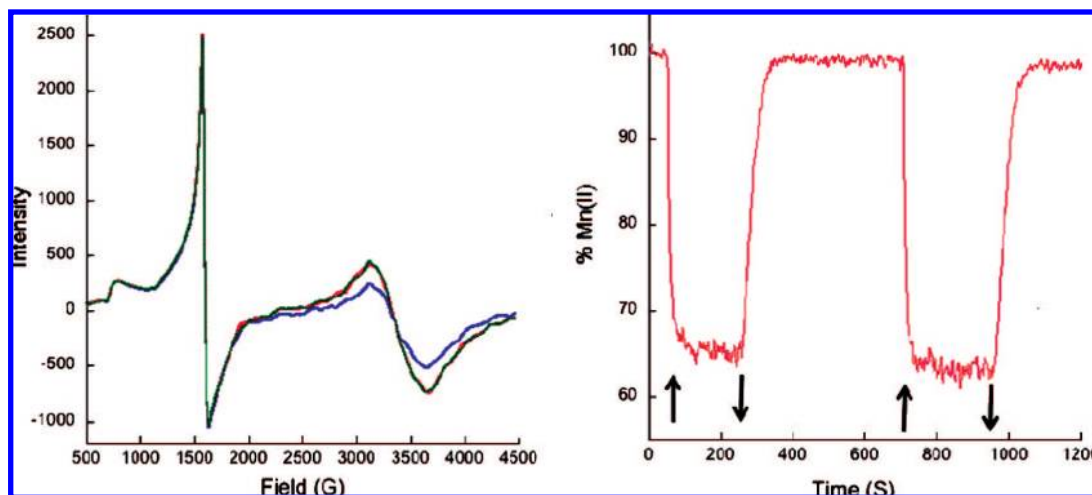
Figure 11. (a) EPR spectra of TiO$_2$ NPs treated with the **2** functionalized with Mn^{II}(OAc)$_2$ in the presence of visible light irradiation (blue) and in dark before (green) and after (red) irradiation. The large signal at 1500 G is attributed to rhombic Fe(III) and serves as an internal control demonstrating that illumination does not heat the sample significantly. (b) Time-dependent intensity at 3106 G with light on (up arrow) and off (down arrow).

determining factor responsible for inducing ultrafast IET from TiO$_2$ surface complexes.[34,45]

3.6. Recombination Dynamics. Figure 11a shows the EPR spectra of colloidal TiO$_2$ films functionalized with [Mn^{II}-(H$_2$O)$_3$(**2**)]$^{2+}$, before, during, and after illumination at 6 K. In the dark, the characteristic signal of Mn(II) is clearly visible (green). After illumination with a broad-spectrum Xe lamp, fitted with a filter transmitting only $\lambda \geq 420$ nm, the Mn(II) signal decays (blue), indicating oxidation to Mn(III). After the lamp is blocked, the Mn(II) signal is regenerated in the absence of electron scavengers (red), indicating reversible photoinduced charge separation.

Figure 11b shows the time-dependent fraction of Mn(II) surface complexes, when turning the light on ($\uparrow$) and off ($\downarrow$) at 6 K. The 23-s time scale for e^-/h^+ recombination at 6 K is much longer than the 1-ms upper limit for carrier trapping and/ or recombination time as measured at room temperature by the THz experiments (using a 1 kHz repetition rate laser, with no residual signal from the previous laser shot detected). Room-temperature EPR was also performed, but no change in signal was detected upon illumination, indicating Mn(III) formation and reduction within the 1-ms time resolution of the EPR measurement, again consistent with the THz results. It is known that e^-/h^+ recombination times are highly temperature-dependent. Future EPR studies at higher temperatures, and THz studies at lower temperatures, will allow us to compare recombination times from both experiments.

4. Conclusions

Derivatized acetylacetonate groups can function as robust anchors and linkers for functionalization of TiO$_2$ surfaces when substituted at the central carbon. These results suggest that suitably modified acac should provide a robust and versatile scaffold for a wide range of transition-metal complexes relevant to photocatalytic and photovoltaic cells. The reported TiO$_2$-acac linkage is more stable to aqueous and oxidative conditions than the classic carboxylate anchors. Acac anchors warrant further study both as applied to photocatalytic oxidation and for the development of dye-sensitized solar cells that are not affected by humidity.

2 has been specifically designed to incorporate the acac-TiO$_2$ binding motif as well as the substituted terpyridine (2,2′:6,2″-terpyridine) ligands common to well-known Mn catalysts for oxidation chemistry.[3,13,46] We find that **2** photosensitizes TiO$_2$ NPs to visible light absorption, is resistant to oxidation because of its low-lying electronic states, and induces favorable directionality of electron transfer because of the positioning of electronic energy levels in the electron donor and acceptor parts of the chromophore ligand.

Simulations of IET into sensitized TiO$_2$ NPs are consistent with THz measurements, providing a detailed molecular level description of possible electron injection mechanisms. Furthermore, there is good agreement between the calculated and measured steady-state UV$-$vis absorption spectra, consistently predicting sensitization of TiO$_2$ NPs to visible light. The relative positioning of the energy levels in the donor and acceptor moieties of the linker favors injection, hinders recombination, and determines rectification properties with subpicosecond IET and recombination times several orders of magnitude longer that the injection time.

In analogy to other sensitized TiO$_2$ materials, the observed stability of the Mn surface complex is correlated with highly efficient charge-separation processes triggered by photoexcitation, including photooxidation of the surface complex and ultrafast IET into the conduction band of TiO$_2$. Regeneration of the initial Mn complex by e^-/h^+ recombination is probably limited by the underlying trapping/detrapping dynamics of the photoinjected electrons within the TiO$_2$ NPs. The EPR studies show it to be on the order of 20 s at 6 K, and the THz experiments bracket it between 500 ps and 1 ms at room temperature.

Prolonged stability of the photooxidized Mn(III) surface complex would be ideally suited for photocatalytic applications, currently under study in our group. However, catalysis at 6 K to take advantage of $\sim$20-s recombination times is clearly not feasible. On the other hand, even recombination times on the order of nanoseconds to hundreds of microseconds at room temperature, which are consistent with the present observations, would allow significant catalytic activity.

(45) Asbury, J. B.; Ellingson, R. J.; Ghosh, H. N.; Ferrere, S.; Nozik, A. J.; Lian, T. Q. *J. Phys. Chem. B* **1999**, *103*, 3110–3119.

(46) (a) Limburg, J.; Vrettos, J. S.; Liable-Sands, L. M.; Rheingold, A. L.; Crabtree, R. H.; Brudvig, G. W. *Science* **1999**, *283*, 1524–1527. (b) Limburg, J.; Vrettos, J. S.; Chen, H.; de Paula, J. C.; Crabtree, R. H.; Brudvig, G. W. *J. Am. Chem. Soc.* **2001**, *123*, 423–430.

Supporting Information Available: Description of the experimental system for THz measurements and EPR methods, structural characterization of the β-ketoester linker, experimental UV−vis, FTIR, and NMR spectra used for characterization of the acac adsorbate, and XRD analysis of Degussa P25 as compared to anatase synthesized by sol−gel methods. This material is available free of charge via the Internet at http://pubs.acs.org.

JA805498W